A Conservative Treatment of
Zonal Boundaries for Euler Equation Calculations

MAN MOHAN RAI

*Informatics General Corporation, Palo Alto, California 94303 at
NASA Ames Research Center, Moffett Field, California 94035*

Finite-difference calculations require the generation of a grid for the region of interest. A zonal approach, wherein the given region is subdivided into zones and the grid for each zone is generated independently, makes the grid-generation process for complicated topologies and for regions requiring selective grid refinement a fairly simple task. This approach results in new boundaries within the given region, that is, zonal boundaries at the interfaces of the various zones. The zonal-boundary scheme (the integration scheme used to update the points on the zonal boundary) for the Euler equations must be conservative, accurate, stable, and applicable to general curvilinear coordinate systems. A zonal-boundary scheme with these desirable properties is developed in this study. The scheme is designed for explicit, first-order-accurate integration schemes but can be modified to accommodate second-order-accurate explicit and implicit integration schemes. Results for inviscid flow, including supersonic flow over a cylinder, blast-wave diffraction by a ramp, and one-dimensional shock-tube flow are obtained on zonal grids. The conservative nature of the zonal-boundary scheme permits the smooth transition of the discontinuities associated with these flows from one zone to another. The calculations also demonstrate the continuity of contour lines across zonal boundaries that can be achieved with the present zonal scheme. © 1986 Academic Press, Inc.

INTRODUCTION

The numerical solution of a partial differential equation using a finite-difference or a finite-element method requires the generation of a grid for the region of interest. The grid-generation process can be quite complicated when the topology of the region itself is complicated (e.g., an aircraft configuration). A second factor that contributes to the complexity of grid generation is the necessity to cluster grid points in regions where the dependent variables and their gradients change rapidly (selective grid refinement).

The use of a zonal approach, wherein the region of interest is divided into a number of zones and a grid is generated for each zone independent of other zones, alleviates both the complex-topology and the selective-grid-refinement problems. Figure 1a shows the flow region associated with a combination of two airfoils. The region is multiply connected and hence difficult to discretize with a single grid system. The division of the flow field into five zones, as in Fig. 1a, results in simple,

472

four-sided regions which can be discretized easily. Figure 1b illustrates how a region requiring selective grid refinement can be discretized with the help of a zonal approach. The shock pattern shown in this figure is a result of the diffraction of a planar shock wave by a ramp. The ramp angle and incident shock Mach number were chosen to yield a double Mach reflection. A very fine mesh is required to resolve the complicated shock structure in zone 1, but a relatively coarse mesh is sufficient to resolve the flow features in zone 2. This change in mesh-point density can be achieved very easily with the help of zonal grids (results of such an approach are presented in a later section).

The division of a given region into zones introduces new boundaries in the calculation: the zonal boundaries. Since the grid for each region is generated
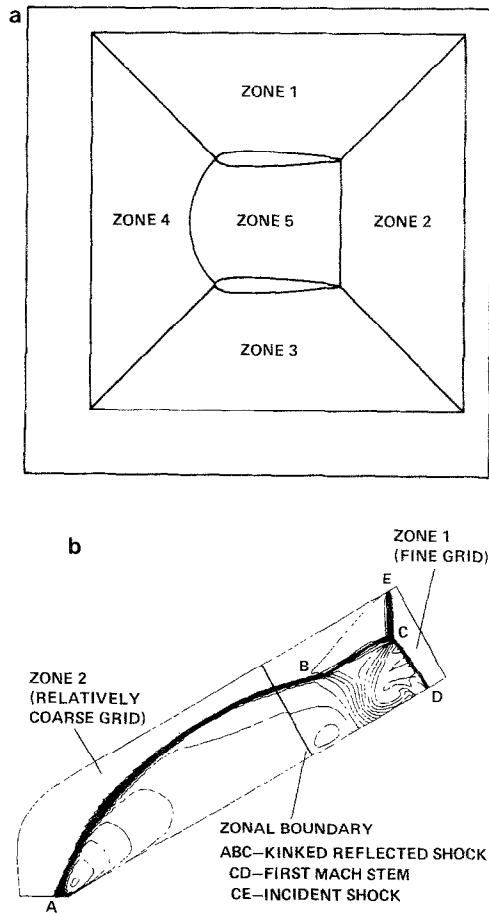

FIG. 1. Use of zonal grids in simplifying grid generation. (a) Zoning of multiply connected region to simplify grid generation process. (b) Zoning of a flow region that requires selective grid refinement.

independently, the grid lines of two adjoining regions may align (continuous grids) or may not align (discontinuous grids) with each other. Even in the case of continuous grids, a sudden change in grid spacing or grid-line orientation across the zonal boundary may give rise to discontinuities in the transformation metrics (metric-discontinuous grids). Figure 2 shows the different types of grids mentioned above. It should be noted that in Figs. 2b–d the adjacent zones meet along a common line and do not overlap; such nonoverlapping grids will be referred to as patched grids in the rest of the paper.

In order that information be transferred from one zone to another accurately, it is important to treat grid points on the zonal boundaries with care. The emphasis in this study is on the proper treatment of zonal boundaries for calculations involving one set of partial differential equations that govern fluid flow: the Euler equations. The nonlinear nature of these equations permits solutions with discontinuities such as shocks and slip surfaces. In order that such discontinuities assume the right strength and physical location it is imperative that the finite-difference scheme used for the calculation be conservative. In a zonal calculation it is important that the zonal boundaries are also treated in a conservative manner so that the discontinuities can move freely across these boundaries. The zonal-boundary condition developed in this study is fully conservative and hence permits the movement of discontinuities across zonal boundaries with minimal distortion of the solution. The scheme is designed for both discontinuous and metric-discontinuous grids.

a CONTINUOUS GRID

b METRIC DISCONTINUOUS GRID

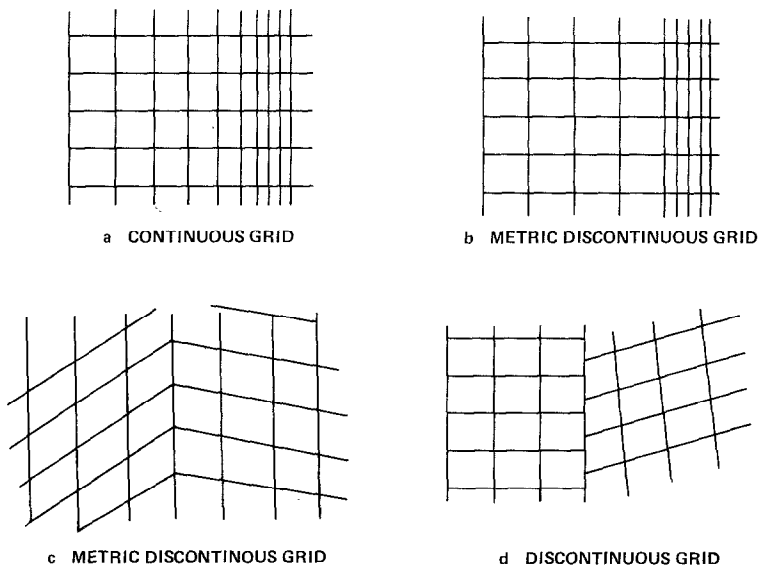c METRIC DISCONTINOUS GRID

d DISCONTINUOUS GRID

FIG. 2. Types of grids used in finite-difference calculations: (a) continuous; (b) metric-discontinuous; (c) metric-discontinuous; (d) discontinuous.

Earlier work in the area of zonal-grid calculations includes that of Cambier *et al.* [1], who analyzed the zonal-boundary problem for a system of hyperbolic equations and used the compatibility equations to develop a zonal-boundary scheme. Good results are presented for transonic channel flow. However, the use of the compatibility equations results in a zonal-boundary scheme that is not conservative and, hence, unsuitable for problems in which flow discontinuities move from one zone to another. Hessenius and Pulliam [2] present a conservative zonal-boundary scheme for implicit integration methods like the Beam–Warming method [3]. Their results stress the need for a conservative zonal-boundary scheme. However, Hessenius and Pulliam do not address the problem of discontinuous metrics or discontinuous grids across zonal boundaries. Rai, Hessenius, and Chakravarthy [4] present results obtained on metric-discontinuous grids; the integration scheme used is the Osher upwind scheme. The proper choice of transformation metrics in the calculation of the fluxes makes the scheme fully conservative at both interior- and zonal-boundary points. Test cases include shocked flow through a nozzle, supersonic flow over a cylinder, and blast-wave diffraction by a ramp. Reference [5] presents a conservative zonal-boundary condition for problems in one spatial dimension. The primary emphasis of this study is the refinement of the mesh in regions of large solution error. In addition to refinement of the grid in space the problem of using different time-steps in different regions is also addressed.

Although [1, 2, 4, 5] present results obtained by integrating the Euler equations on zonal grids, related work has also been done using the transonic full-potential equation. Typical of this effort is the work of Atta [6] and Atta and Vadyak [7]. The approach in [6, 7], though zonal, does not use the patched-grid concept (the present study deals exclusively with patched grids) but instead uses the overlaid grid concept, that is, the zones used in the calculation overlap. An advantage of this approach is that zones need not match perfectly with their neighbors. Reference [8] gives results obtained on overlaid grids in conjunction with the stream-function approach.

Some disadvantages of overlaid grids are

(1) a problem in n spatial dimensions requires interpolation in n dimensions (to transfer information from one grid onto another), whereas patched grids require only an $(n-1)$-dimensional interpolation (the details are given in a later section);

(2) maintaining global conservation seems to be more difficult with overlaid grids; and

(3) the accuracy and convergence speed of the calculation seems to depend on the degree of overlap of the zones and the relative size of each zone [6], thus introducing a certain amount of undesirable empiricism in the formulation.

However, the fact that zones can (and should) overlap, may result in a certain amount of flexibility in generating grids in three dimensions. A second advantage of overlaid grids may lie in the ease with which grids can be moved relative to each other (for calculations involving bodies that move relative to each other).

References [9, 10] give patched-grid results for the potential and full-potential equations; the problem of conservation of fluxes is not addressed.

A zonal-boundary scheme for patched grids is developed in the next section. It is designed for explicit, first-order-accurate integration schemes. The integration schemes used in this study are the Osher [11] and the split-flux [12] schemes. The zonal-boundary scheme is fully conservative and has been found to be stable and accurate even under severe test conditions such as strong discontinuities passing through zonal boundaries. The use of the present zonal-boundary scheme does not affect the convergence rate of the calculation relative to a single-zone calculation.

Results are presented for the cases of supersonic flow over a cylinder, blast-wave diffraction by a ramp, and the one-dimensional shock-tube problem solved on a two-dimensional grid. The captured discontinuities are oscillation-free because of the first-order accuracy of the integration schemes, and, in the case of the Osher scheme, the discontinuities are also very sharp. The discontinuities were found to move freely across zonal boundaries.

THE ZONAL-BOUNDARY SCHEME

Consider the unsteady Euler equations in two dimensions:

$$Q_t + E_x + F_y = 0. \tag{1}$$

The vectors Q, E, and F are given by

$$Q = \begin{bmatrix} \rho \\ \rho u \\ \rho v \\ e \end{bmatrix}, \qquad E = \begin{bmatrix} \rho u \\ p + \rho u^2 \\ \rho u v \\ (e+p) u \end{bmatrix}, \qquad F = \begin{bmatrix} \rho v \\ \rho u v \\ p + \rho v^2 \\ (e+p) v \end{bmatrix}, \tag{2}$$

where ρ is the density, p is the pressure, u and v are the velocities in the x and y directions, respectively, and e is the total energy per unit volume. An explicit conservative finite-difference scheme for Eq. (1) can be written as

$$\frac{Q_{j,k}^{n+1} - Q_{j,k}^n}{\Delta t} + \frac{\hat{E}_{j+1/2,k} - \hat{E}_{j-1/2,k}}{\Delta x} + \frac{\hat{F}_{j,k+1/2} - \hat{F}_{j,k-1/2}}{\Delta y} = 0, \tag{3}$$

where $\hat{E}_{j+1/2,k}$ and $\hat{F}_{j,k+1/2}$ are numerical fluxes that are consistent with the physical fluxes E and F and are evaluated at the nth time-level. The region of interest being considered is shown in Fig. 3. Equation (3) can be alternatively written as

$$\frac{\Delta x\, \Delta y}{\Delta t} (Q_{j,k}^{n+1} - Q_{j,k}^n) + \Delta y(\hat{E}_{j+1/2,k} - \hat{E}_{j-1/2,k}) + \Delta x(\hat{F}_{j,k+1/2} - \hat{F}_{j,k-1/2}) = 0. \tag{4}$$
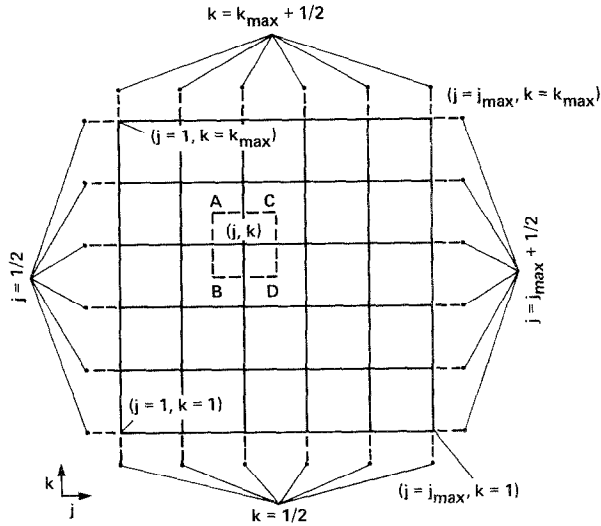
FIG. 3. Grid to illustrate global conservation property of conservative difference operators.

In this form the various terms in the equation can be easily interpreted; for example, the first term

$$\frac{\Delta x\, \Delta y}{\Delta t}\, (Q_{j,k}^{n+1} - Q_{j,k}^{n})$$

represents the rate of increase of the variable $Q_{j,k}$ in the cell $ABCD$ (Fig. 3). The term

$$-\Delta y(\hat{E}_{j+1/2,k} - \hat{E}_{j-1/2,k})$$

represents the net influx of mass, momentum, and energy into the cell through the sides AB and CD, and the term

$$-\Delta x(\hat{F}_{j,k+1/2} - \hat{F}_{j,k-1/2})$$

represents the net influx of the same quantities through the sides AC and BD.
    A summation of the term

$$\frac{\Delta x\, \Delta y}{\Delta t}\, (Q_{j,k}^{n+1} - Q_{j,k}^{n})$$

overall grid points yields [using Eq. (4)]

$$S = \sum_{j=1}^{j\max} \sum_{k=1}^{k\max} \frac{\Delta x\, \Delta y}{\Delta t} (Q_{j,k}^{n+1} - Q_{j,k}^{n})$$

$$= \Delta x \sum_{j=1}^{j\max} (\hat{F}_{j,1/2} - \hat{F}_{j,k\max+1/2})$$

$$+ \Delta y \sum_{k=1}^{k\max} (\hat{E}_{1/2,k} - \hat{E}_{j\max+1/2,k}). \tag{5}$$

That is, S is only a sum of the boundary fluxes; the interior fluxes cancel each other out because the difference scheme [Eq. (3)] is conservative. Equation (5) represents the global-conservation property of any scheme that can be represented as in Eq. (3).

Consider the grids shown in Fig. 4. The line AB represents the zonal boundary that separates the two grids that are used to discretize the given region. Let l and m be the indices used in the x and y directions, respectively, in zone 1 and let j and k be the corresponding indices for zone 2. Note that m and k increase in opposite directions. This choice of indices was made to simplify the notation used to develop the zonal-boundary scheme and need not be adhered to in a general zonal code. Let n represent the time-step for both zones. A superscript within parentheses will denote the zone to which a given quantity belongs; for example, $\Delta x^{(1)}$ denotes the mesh spacing in the x direction in zone 1.

One condition that must be satisfied across the zonal boundary is the continuity of the dependent variables. This condition can be easily satisfied by integrating the equations of motion to update Q on one side of the zonal boundary and interpolating these variables to obtain the updated variables on the other side of the
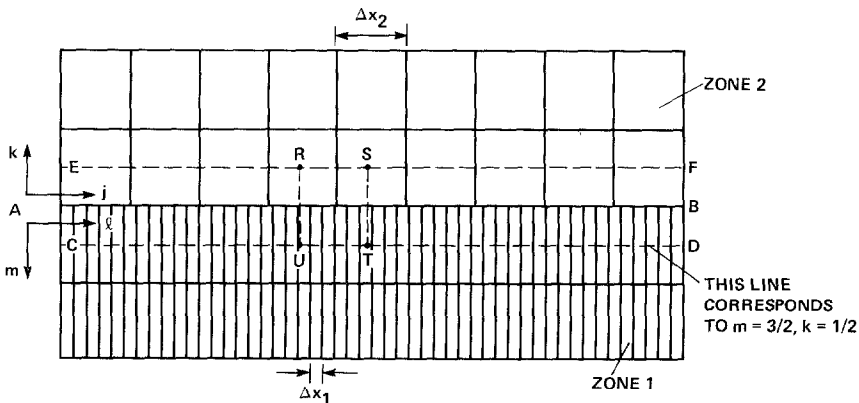

FIG. 4. Two-zone grid to illustrate zonal scheme in Cartesian coordinates.

zonal boundary. This interpolation results in the dependent variables being continuous (across the zonal boundary) to the order of accuracy of the interpolation scheme. A linear interpolation scheme was used to obtain the results presented in this study.

Assume that the zonal-boundary points of zone 2 are to be updated using the finite-difference scheme of Eq. (3). This calculation requires the fluxes $\hat{F}^{(2)}_{j,1/2}$. The question of how to calculate these fluxes introduces the second condition that is to be satisfied at the zonal boundary in a natural way; that is, these fluxes have to be calculated such that global conservation is maintained. In other words, a summation of $[\Delta x^{(1)} \Delta y^{(1)} / \Delta t] \Delta Q^{(1)}_{l,m}$ and $[\Delta x^{(2)} \Delta y^{(2)} / \Delta t] \Delta Q^{(2)}_{j,k}$ over all the cells in the region of interest [as was done in Eq. (5)] should once again result in only the boundary fluxes. The sum should not contain any residual fluxes near the zonal boundary. Note that cells corresponding to the zonal-boundary points of zone 1 are not to be included in this summation. This is because the area that these cells represent has already been accounted for with the inclusion of the cells corresponding to the zonal-boundary points of zone 2 (a sum of the cell areas included in the above summation should result in the total area covered by the two zones). A typical cell ($RSTU$) of a zonal-boundary point (j, 1) is shown in Fig. 4. The points R and S are midpoints of the cells in which R and S lie, and the points T and U are obtained as follows: The constant j lines of zone 2 are extrapolated into zone 1 to intersect the line CD (CD correspond to $m = \frac{3}{2}$ in zone 1 and $k = \frac{1}{2}$ in zone 2). The intersection points have the indices ($j, \frac{1}{2}$). Point T is midway between the points ($j+1, \frac{1}{2}$) and ($j, \frac{1}{2}$), and point U is midway between points ($j, \frac{1}{2}$) and ($j - 1, \frac{1}{2}$).

The global-conservation property can be shown to be satisfied if the following relationship is satisfied:

$$\frac{\Delta x^{(2)}}{2} \left[\hat{F}^{(2)}_{1,1/2} + \hat{F}^{(2)}_{j\max,1/2} \right] + \Delta x^{(2)} \sum_{j=2}^{j\max - 1} \hat{F}^{(2)}_{j,1/2}$$

$$= \frac{\Delta x^{(1)}}{2} \left[\hat{F}^{(1)}_{1,3/2} + \hat{F}^{(1)}_{l\max,3/2} \right] + \Delta x^{(1)} \sum_{l=2}^{l\max - 1} \hat{F}^{(1)}_{l,3/2}. \tag{6}$$

A close examination of Eq. (6) shows that each side of this equation is nothing but a discrete form of the line integral of the numerical flux $\hat{F}$ along the line CD in Fig. 4, and the equation itself represents flux conservation across the zonal boundary. Equation (6) is only a necessary condition and is not sufficient to define the fluxes $\hat{F}^{(2)}_{j,1/2}$ in a physically meaningful way [the $\hat{F}^{(2)}_{j,1/2}$ cannot be obtained from Eq. (6) alone since Eq. (6) does not uniquely specify the $\hat{F}^{(2)}_{j,1/2}$].

Assume that the $\hat{F}^{(2)}_{j,1/2}$ are obtained by interpolating the $\hat{F}^{(1)}_{l,3/2}$; that is,

$$\hat{F}^{(2)}_{j,1/2} = \sum_{l=p}^{q} N_{j,l} \hat{F}^{(1)}_{l,3/2}, \tag{7}$$

where the $N_{j,l}$ are interpolation coefficients and p and q define the set of fluxes of zone 1 that will be used in the interpolation. The third and final condition to be met at the zonal boundary (one that is fundamental to the interpolation being carried out) is that

$$\sum_{l=p}^{q} N_{j,l} = 1. \tag{8}$$

We now describe a very simple way of obtaining the interpolation coefficients $N_{j,l}$ such that Eqs. (6) and (8) are automatically satisfied. Let the line CD in Fig. 5 correspond to the line CD in Fig. 4. The dots (Fig. 5) represent the grid points of zone 1 and the crosses represent those of zone 2. Representative numerical values of $\hat{F}_{l,3/2}^{(1)}$ are plotted on the positive y axis. Assume a piecewise, constant variation of $\hat{F}_{l,3/2}^{(1)}$, that is, $\hat{F}_{l,3/2}^{(1)}$ is constant between $x_{l-1/2,3/2}^{(1)}$ and $x_{l+1/2,3/2}^{(1)}$. Consider a point of zone 2, $(j, \frac{1}{2})$. Let E be midway between $(j-1, \frac{1}{2})$ and $(j, \frac{1}{2})$ and F be midway between $(j, \frac{1}{2})$ and $(j+1, \frac{1}{2})$. The $\hat{F}_{j,1/2}^{(2)}$ are now calculated from

$$\Delta x^{(2)} \hat{F}_{j,1/2}^{(2)} = \int_{E}^{F} \hat{F}_{l,3/2}^{(1)} \, dx$$

or

$$\hat{F}_{j,1/2}^{(2)} = \frac{1}{\Delta x^{(2)}} \int_{E}^{F} \hat{F}_{l,3/2}^{(1)} \, dx$$

$$= \sum_{l=p}^{q} N_{j,l} \hat{F}_{l,3/2}^{(1)}, \tag{9}$$

where the values of $N_{j,l}$ are given by

$$N_{j,l} = \begin{cases} 0 & \text{if } x_{l+1/2}^{(1)}, x_{l-1/2}^{(1)} \leqslant x_{j-1/2}^{(2)} \\ 0 & \text{if } x_{l+1/2}^{(1)}, x_{l-1/2}^{(1)} \geqslant x_{j+1/2}^{(2)} \\ \dfrac{[\min(x_{j+1/2}^{(2)}, x_{l+1/2}^{(1)}) - \max(x_{j-1/2}^{(2)}, x_{l-1/2}^{(1)})]}{x_{j+1/2}^{(2)} - x_{j-1/2}^{(2)}} & \text{otherwise.} \end{cases} \tag{10}$$
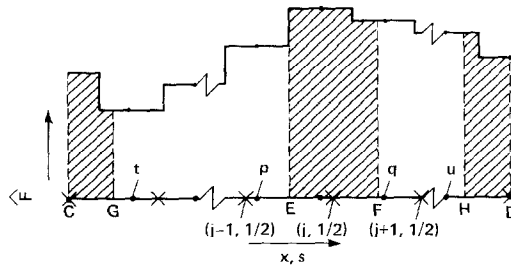

FIG. 5. Piecewise constant variation of the numerical flux $\hat{F}$ as a function of x or s.

The simple expressions for $N_{j,l}$ in Eq. (10) are valid only for a piecewise constant variation of the numerical fluxes. A piecewise linear or any other variation would result in different formulae for the $N_{j,l}$. Equation (10) in an indirect manner, also yields the endpoints in the interpolation, p and q (p and q include only that set of fluxes of zone 1 that are multiplied by a nonzero interpolation coefficient for a given flux of zone 2). The end fluxes $\hat{F}^{(2)}_{1,1/2}$ and $\hat{F}^{(2)}_{j\max,1/2}$ are calculated as

$$\hat{F}^{(2)}_{1,1/2} = \frac{2}{\Delta x^{(2)}} \int_C^G \hat{F}^{(1)}_{l,3/2} \, dx,$$

$$\hat{F}^{(2)}_{j\max,1/2} = \frac{2}{\Delta x^{(2)}} \int_H^D \hat{F}^{(1)}_{l,3/2} \, dx. \tag{11}$$

The fluxes thus obtained satisfy Eq. (6) automatically, and the interpolation coefficients defined by Eqs. (9)–(11) satisfy Eq. (8). The shaded areas in Fig. 5 represent the values of the integrals in Eqs. (9) and (11).

The foregoing discussion pertained to simple rectangular grids. The treatment of the zonal-boundary points was reduced to

(1) updating the points of zone 2 using a specified difference scheme, and

(2) updating the points of zone 1 by interpolating the dependent variables at the grid points of zone 2.

The fluxes used to update the zonal points of zone 2 were obtained using a "conservative interpolation technique" that satisfied flux conservation across the zonal boundary. The extension of the method to arbitrary curvilinear grid systems is straightforward and is outlined below.

Consider the curvilinear grids used to discretize the region shown in Fig. 6. Establishing two independent-variable transformations

$$\tau^{(i)} = t,$$

$$\xi^{(i)} = \xi^{(i)}(x, y, t), \qquad i = \begin{cases} 1 & \text{for zone 1} \\ 2 & \text{for zone 2} \end{cases} \tag{12}$$

$$\eta^{(i)} = \eta^{(i)}(x, y, t),$$

and applying these transformations to Eq. (1) we obtain

$$\tilde{Q}^{(i)}_{\tau^{(i)}} + \tilde{E}^{(i)}_{\xi^{(i)}} + \tilde{F}^{(i)}_{\eta^{(i)}} = 0, \qquad i = 1, 2, \tag{13}$$

where

$$\tilde{Q}^{(i)} = Q/J^{(i)},$$

$$\tilde{E}^{(i)}[Q, \xi^{(i)}] = [\xi_t^{(i)} Q + \xi_x^{(i)} E + \xi_y^{(i)} F]/J^{(i)},$$

$$\tilde{F}^{(i)}[Q, \eta^{(i)}] = [\eta_t^{(i)} Q + \eta_x^{(i)} E + \eta_y^{(i)} F]/J^{(i)}, \tag{14}$$

$$J^{(i)} = \xi_x^{(i)} \eta_y^{(i)} - \eta_x^{(i)} \xi_y^{(i)}.$$

The notation $\tilde{E}^{(i)}[Q, \xi^{(i)}]$ and $\tilde{F}^{(i)}[Q, \eta^{(i)}]$ is used to show the dependence of these quantities on the metrics of the transformation. Let the conservative difference schemes used to integrate Eq. (13) be given by

$$\frac{\Delta \tilde{Q}_{l,m}^{(1)}}{\Delta \tau^{(1)}} + \frac{\hat{E}_{l+1/2,m}^{(1)} - \hat{E}_{l-1/2,m}^{(1)}}{\Delta \xi^{(1)}} + \frac{\hat{F}_{l,m+1/2}^{(1)} - \hat{F}_{l,m-1/2}^{(1)}}{\Delta \eta^{(1)}} = 0 \qquad (15)$$

and

$$\frac{\Delta \tilde{Q}_{j,k}^{(2)}}{\Delta \tau^{(2)}} + \frac{\hat{E}_{j+1/2,k}^{(2)} - \hat{E}_{j-1/2,k}^{(2)}}{\Delta \xi^{(2)}} + \frac{\hat{F}_{j,k+1/2}^{(2)} - \hat{F}_{j,k-1/2}^{(2)}}{\Delta \eta^{(2)}} = 0, \qquad (16)$$

where $\hat{E}^{(i)}$ and $\hat{F}^{(i)}$ are, once again, numerical fluxes but are consistent with the transformed fluxes $\tilde{E}^{(i)}$ and $\tilde{F}^{(i)}$. The interior points of each zone are updated using the appropriate metrics and dependent variables. At the zonal boundary, once again, the grid points of one zone are updated by integrating the equations of motion (say, zone 2) and those in the other zone (say, zone 1) are updated by interpolating the dependent variables of the first zone.

A typical cell $RSTU$ associated with the zonal boundary point $(j, 1)$ of zone 2 is shown in Fig. 6. The points R, S, T, and U are defined as in the previous case. The metrics of the transformation at the point $(j, 1)$ are defined in a manner consistent with the shape and size of the cell $RSTU$, that is,

$$[x_{\eta^{(2)}}]_{j,1} = x_{j,3/2}^{(2)} - x_{j,1/2}^{(2)},$$

$$[y_{\eta^{(2)}}]_{j,1} = y_{j,3/2}^{(2)} - y_{j,1/2}^{(2)},$$

$$[x_{\xi^{(2)}}]_{j,1} = [x_{j+1,1}^{(2)} - x_{j-1,1}^{(2)}]/2,$$

$$[y_{\xi^{(2)}}]_{j,1} = [y_{j+1,1}^{(2)} - y_{j-1,1}^{(2)}]/2,$$

$$x_{j,3/2}^{(2)} = [x_{j,2}^{(2)} + x_{j,1}^{(2)}]/2,$$

$$y_{j,3/2}^{(2)} = [y_{j,2}^{(2)} + y_{j,1}^{(2)}]/2.$$

Flux conservation across the line CD (as in the previous case) requires that the following condition be satisfied:

$$\tfrac{1}{2}[\hat{F}_{1,1/2}^{(2)} + \hat{F}_{j\max,1/2}^{(2)}] + \sum_{j=2}^{j\max-1} \hat{F}_{j,1/2}^{(2)} = \tfrac{1}{2}[\hat{F}_{1,3/2}^{(1)} + \hat{F}_{l\max,3/2}^{(1)}] + \sum_{l=2}^{l\max-1} \hat{F}_{l,3/2}^{(1)}. \qquad (17)$$

Equation (17) assumes that $\Delta \xi^{(i)}$ and $\Delta \eta^{(i)} = 1$. To satisfy Eq. (17), a running parameter s is established along the line CD. The quantity s represents the distance of a point from the point C along the curve CD. Figure 5 shows the line CD stretched into a straight line along the s axis. Representative numerical values of $\hat{F}_{l,3/2}^{(1)}$ are plotted on the positive y axis and a piecewise constant variation of $\hat{F}_{l,3/2}^{(1)}$ is
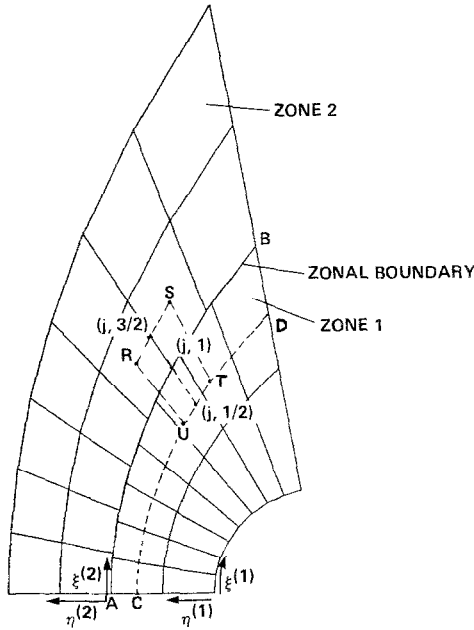
FIG. 6. Two-zone grid to illustrate zonal scheme in curvilinear coordinates.

assumed as before. Defining the points E and F as before, Eq. (17) can be satisfied exactly by evaluating $\hat{F}^{(2)}_{j,1/2}$ from

$$\hat{F}^{(2)}_{j,1/2}[Q, \eta^{(2)}_{j,1/2}] = \int_E^F \frac{\hat{F}^{(1)}_{l,3/2}[Q, \eta^{(1)}_{l,3/2}] \, ds}{[s^{(1)}_{l+1/2} - s^{(1)}_{l-1/2}]}$$

$$= [s^{(2)}_{j+1/2} - s^{(2)}_{j-1/2}] \sum_{l=p}^{q} N_{j,l} \frac{\hat{F}^{(1)}_{l,3/2}[Q, \eta^{(1)}_{l,3/2}]}{[s^{(1)}_{l+1/2} - s^{(1)}_{l-1/2}]}. \tag{18}$$

The $N_{j,l}$ can be shown to satisfy Eq. (8). The term $[s^{(1)}_{l+1/2} - s^{(1)}_{l-1/2}]$ in the denominator of the integral in Eq. (18) serves to convert the numerical flux $\hat{F}^{(1)}_{l,3/2}$ into a flux per unit length (the metrics contained within the numerical flux take the length of the side of the cell into account). The integration process reintroduces a length parameter. Equation (18) can be made very similar to Eq. (9) by making the following approximations:

$$s^{(1)}_{l+1/2} - s^{(1)}_{l-1/2} \simeq [(x_{\xi^{(1)}})^2_{l,3/2} + (y_{\xi^{(1)}})^2_{l,3/2}]^{1/2} + O[\Delta\xi^{(1)}]^2$$

and

$$s^{(2)}_{j+1/2} - s^{(2)}_{j-1/2} \simeq [(x_{\xi^{(2)}})^2_{j,1/2} + (y_{\xi^{(2)}})^2_{j,1/2}]^{1/2} + O[\Delta\xi^{(2)}]^2. \tag{19}$$

Defining

$$\hat{\bar{F}}^{(1)}_{l,3/2}[Q, \eta^{(1)}_{l,3/2}] = \frac{\bar{F}^{(1)}_{l,3/2}[Q, \eta^{(1)}_{l,3/2}]}{[(x_{\xi^{(1)}})^2_{l,3/2} + (y_{\xi^{(1)}})^2_{l,3/2}]^{1/2}},$$

$$\hat{\bar{F}}^{(2)}_{j,1/2}[Q, \eta^{(2)}_{j,1/2}] = \frac{\bar{F}^{(2)}_{j,1/2}[Q, \eta^{(2)}_{j,1/2}]}{[(x_{\xi^{(2)}})^2_{j,1/2} + (y_{\xi^{(2)}})^2_{j,1/2}]^{1/2}}, \tag{20}$$

and making use of the approximations in Eq. (19), Eq. (18) can be written as

$$\hat{\bar{F}}^{(2)}_{j,1/2}[Q, \eta^{(2)}_{j,1/2}] = \frac{1}{[s^{(2)}_{j+1/2} - s^{(2)}_{j-1/2}]} \int_E^F \hat{\bar{F}}^{(1)}_{l,3/2}[Q, \eta^{(1)}_{l,3/2}] \, ds$$

$$= \sum_{l=p}^{q} N_{j,l} \hat{\bar{F}}^{(1)}_{l,3/2}[Q, \eta^{(1)}_{l,3/2}], \tag{21}$$

The analogy between Eqs. (9) and (18) is now apparent via Eq. (21). It should be noted that although the preceding approximations help to clarify the analogy between Eqs. (9) and (18), they are not required for the development of the theory. The end fluxes $\hat{F}^{(2)}_{1,1/2}$ and $\hat{F}^{(2)}_{j\max,1/2}$ can now be obtained in a similar manner from

$$\hat{\bar{F}}^{(2)}_{1,1/2}[Q, \eta^{(2)}_{1,1/2}] = \frac{2}{[s^{(2)}_{3/2} - s^{(2)}_1]} \int_C^G \hat{\bar{F}}^{(1)}_{l,3/2}[Q, \eta^{(1)}_{l,3/2}] \, ds,$$

$$\hat{\bar{F}}^{(2)}_{j\max,1/2}[Q, \eta^{(2)}_{j\max,1/2}] = \frac{2}{[s^{(2)}_{j\max} - s^{(2)}_{j\max-1/2}]} \int_H^D \hat{\bar{F}}^{(1)}_{l,3/2}[Q, \eta^{(1)}_{l,3/2}] \, ds. \tag{22}$$

The preceding method of obtaining the $\hat{F}^{(2)}_{j,1/2}$ [Eq. (18)] is not free-stream preserving. However, a repeated integration of the governing equations with free-stream conditions everywhere (as initial conditions) and without boundary conditions on a grid of the type shown in Fig. 6 resulted in only a 0.1 % drift in the density in the vicinity of the zonal boundary. It can be shown (see Appendix) that the drift in free-stream conditions near the zonal boundary is proportional to the curvature of the zonal boundary and is caused by terms that are second order in magnitude. Hence, it behooves the user to use zonal boundaries with moderate curvature.

The zonal-boundary technique has thus far been developed for a region divided into two adjacent zones. The technique, however, is not restricted to two-zone calculations but can be generalized to an arbitrary number of zones positioned arbitrarily with respect to each other. As an example of using multiple zones, the region shown in Fig. 7 is divided into four zones with the use of three zonal boundaries. The lines along which a flux balance is carried out are AC, FG, DC, and EB. The shaded areas depict typical cell areas for points situated on the zonal boundaries. Grid points that belong to only one zonal boundary usually have four-sided
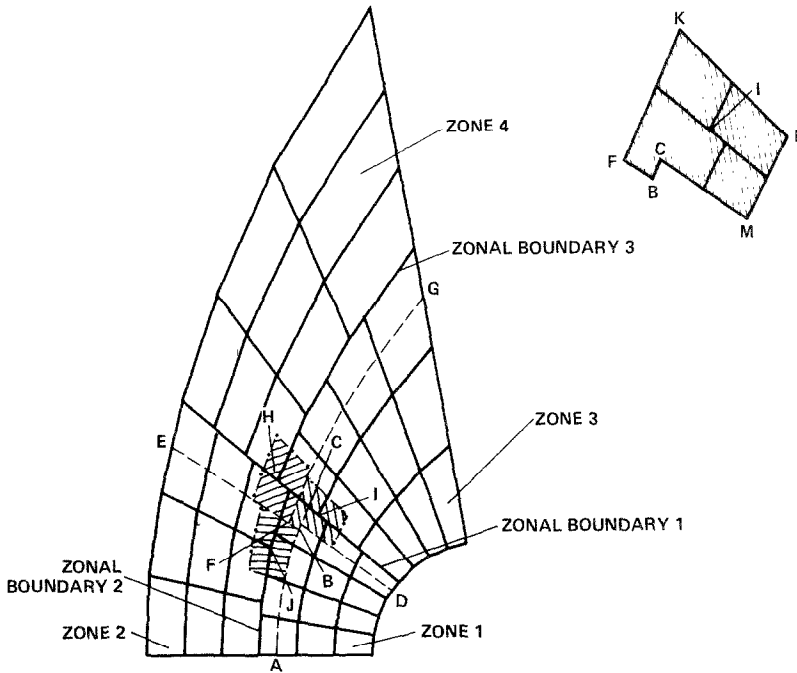
FIG. 7. Four-zone grid to illustrate zonal scheme in curvilinear coordinates.

cell areas. However, zonal grid points that are close to the intersection of two or more zonal boundaries may sometimes be required to have cell areas that are bounded by more than four sides (point I in Fig. 7). These nonstandard cell shapes are required to cover the entire region by cell areas corresponding to grid points that are updated by integrating the equations of motion. The cell areas corresponding to zonal-boundary points can be easily determined, once the lines along which a flux balance is carried out are established.

The first step in a zonal calculation (after the zones have been established and a grid has been generated for each zone) is to determine the lines along which a flux balance will be carried out. Fig. 7 shows one particular choice of "flux balance lines." Table I lists the ways in which zonal boundary points of each zone are updated for this choice of flux balance lines. It was found that for the first-order accurate integration schemes used in this study the choice of flux-balance lines has very little effect on the accuracy of the solution. The next step is to establish distance parameters (like s in the preceding development) along each of the flux-balance lines. The interior points are then updated, using a standard integration scheme, and the zonal-boundary points that have four-sided cell areas are updated, using the integrals developed earlier.

Zonal-boundary points that have cell areas that are bounded by more than four

TABLE I

Type of Update for the Zonal-Boundary Points of Each Zone

Zone No.	Zonal boundary No.	Type of update	Zonal boundary No.	Type of update
1	1	Interpolation	2	Interpolation
2	1	Interpolation	2	Integration
3	1	Integration	3	Interpolation
4	1	Integration	3	Integration

sides require a special definition of the fluxes used in the integration. Consider the point I in Fig. 7. Assume that the indices of this point are (j, k), j in the ξ-direction and k in the η-direction. The fluxes $\hat{E}^{(3)}_{j+1/2,k}[Q, \xi^{(3)}_{j+1/2,k}]$, $\hat{F}^{(3)}_{j,k-1/2}[Q, \eta^{(3)}_{j,k-1/2}]$, and $\hat{F}^{(3)}_{j,k+1/2}[Q, \eta^{(3)}_{j,k+1/2}]$ are easily available. The metrics $\xi^{(3)}_{j+1/2,k}$, $\eta^{(3)}_{j,k-1/2}$, and $\eta^{(3)}_{j,k+1/2}$ are obtained using the sides KL, LM, and FK, respectively, and central differences, for example,

$$[x_{\xi^{(3)}}]_{j,k+1/2} = (x)_K - (x)_F.$$

The flux $\hat{E}^{(3)}_{j-1/2,k}[Q, \xi^{(3)}_{j-1/2,k}]$ is evaluated from

$$\hat{E}^{(3)}_{j-1/2,k}[Q, \xi^{(3)}_{j-1/2,k}] = \int_M^C \hat{\tilde{E}}(Q, \xi)\, ds + \int_B^F \hat{\tilde{E}}(Q, \xi)\, ds. \qquad (23)$$

To account for the side BC, the modified flux $\bar{\hat{F}}^{(3)}_{j,k-1/2}[Q, \eta^{(3)}_{j,k-1/2}]$ is used instead of $\hat{F}^{(3)}_{j,k-1/2}[Q, \eta^{(3)}_{j,k-1/2}]$ in the integration scheme. The modified flux is given by

$$\bar{\hat{F}}^{(3)}_{j,k-1/2}[Q, \eta^{(3)}_{j,k-1/2}] = \hat{F}^{(3)}_{j,k-1/2}[Q, \eta^{(3)}_{j,k-1/2}] + \int_B^C \hat{\tilde{F}}(Q, \eta)\, ds. \qquad (24)$$

INTEGRATION SCHEMES

The previous section dealt with the conservative treatment of zonal boundaries. It was assumed that a conservative finite-difference scheme, for which the numerical fluxes $\hat{E}_{j+1/2,k}$ and $\hat{F}_{j,k+1/2}$ were easily defined, was available. The results in this study were obtained with the first-order-accurate versions of the Osher scheme and the split-flux scheme of Steger and Warming. The definitions of the numerical fluxes for the two schemes are given in this section.

$$\hat{E}_{j+1/2,k} = \frac{1}{2}\left[\tilde{E}(Q_{j,k}, \xi_{j+1/2,k}) + \tilde{E}(Q_{j+1,k}, \xi_{j+1/2,k}) - \int_{Q_{j,k}}^{Q_{j+1,k}} \left|\frac{\partial \tilde{E}}{\partial Q}(Q, \xi_{j+1/2,k})\right| dQ \right],$$

$$\hat{F}_{j,k+1/2} = \frac{1}{2}\left[\tilde{F}(Q_{j,k}, \eta_{j,k+1/2}) + \tilde{F}(Q_{j,k+1}, \eta_{j,k+1/2}) - \int_{Q_{j,k}}^{Q_{j,k+1}} \left|\frac{\partial \tilde{F}}{\partial Q}(Q, \eta_{j,k+1/2})\right| dQ \right].$$

$$(25)$$

The integrals are evaluated along subpaths in state space that are parellel to the right eigenvectors of the matrices $\partial \tilde{E}/\partial Q$ and $\partial \tilde{F}/\partial Q$. The "+" subintegrals along each subpath are identically zero if the corresponding eigenvalue is negative all along the subpath and the "−" subintegrals are identically zero if the corresponding eigenvalue is positive throughout the path. These integrals (when they are not zero) can be shown to be simply evaluated as the difference in fluxes between the end points of the associated subpath. Details of the scheme can be found in [4, 11].

The numerical fluxes for the split-flux scheme can be easily written as

$$\hat{E}_{j+1/2,k} = \tilde{E}^{-}(Q_{j+1,k}, \xi_{j+1/2,k}) + \tilde{E}^{+}(Q_{j,k}, \xi_{j+1/2,k});$$

$$\hat{F}_{j,k+1/2} = \tilde{F}^{-}(Q_{j,k+1}, \eta_{j,k+1/2}) + \tilde{F}^{+}(Q_{j,k}, \eta_{j,k+1/2}),$$

$$(26)$$

where

$$\tilde{E}^{+} = \left(\frac{\partial \tilde{E}}{\partial \tilde{Q}}\right)^{+} \tilde{Q},$$

$$\tilde{E}^{-} = \left(\frac{\partial \tilde{E}}{\partial \tilde{Q}}\right)^{-} \tilde{Q},$$

$$(27)$$

and $\tilde{F}^{+}$ and $\tilde{F}^{-}$ are defined similarly. Further details of the scheme can be found in [12].

The metrics at the half points $(j+1/2, k)$ and $(j, k+1/2)$ are evaluated using the following averaging technique

$$(x_{\eta})_{j+1/2,k} = \tfrac{1}{2}[(x_{\eta})_{j,k} + (x_{\eta})_{j+1,k}],$$

$$(x_{\xi})_{j,k+1/2} = \tfrac{1}{2}[(x_{\xi})_{j,k} + (x_{\xi})_{j,k+1}],$$

$$(28)$$

where the $(x_{\xi})_{j,k}$, $(x_{\xi})_{j,k+1}$, $(x_{\eta})_{j,k}$, and $(x_{\eta})_{j+1,k}$ are evaluated using central differences. The derivatives of y at the half points can be obtained by replacing x with y in Eqs. (28).

RESULTS

Results are presented in this section for inviscid problems in two dimensions. The test cases include supersonic flow past a cylinder, blast wave diffraction by a ramp, and the one-dimensional shock-tube problem solved on a two-dimensional grid. The first-order-accurate versions of the Osher and split-flux schemes are used to integrate the equations of motion at the interior points of the grids, and the zonal-boundary scheme described earlier is used to update the points on the zonal boundaries.

Cylinder in a Supersonic Free Stream

The first problem solved was that of a cylinder in a supersonic free stream ($M_\infty = 2$) with the associated bow shock. Figure 8 shows the grid used for the calculation. The region of interest was divided into two zones separated by the zonal-boundary AB. The discontinuity of the constant-ξ grid lines at the zonal boundary is evident. The values of the dependent variables at all the grid points were set equal to their free-stream values initially. The equations of motion together with the various boundary conditions were integrated (including the zonal-boundary conditions) until the solution converged to its steady-state value. Figure 9 shows the pressure contours obtained at convergence with the Osher scheme. The
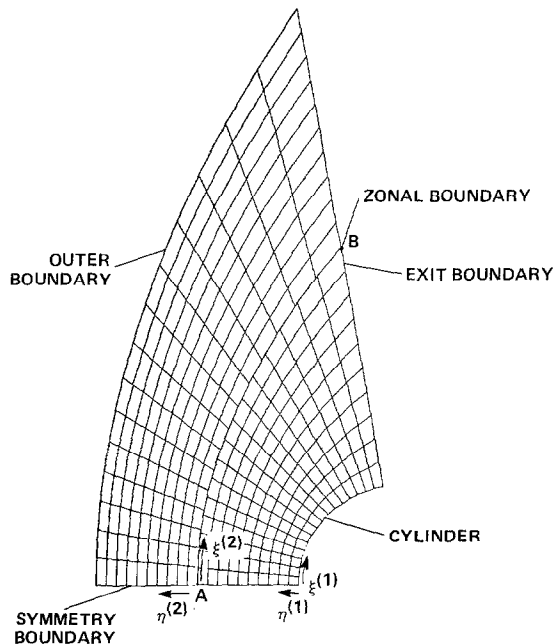
FIG. 8.   Grid for two-zone cylinder calculation.
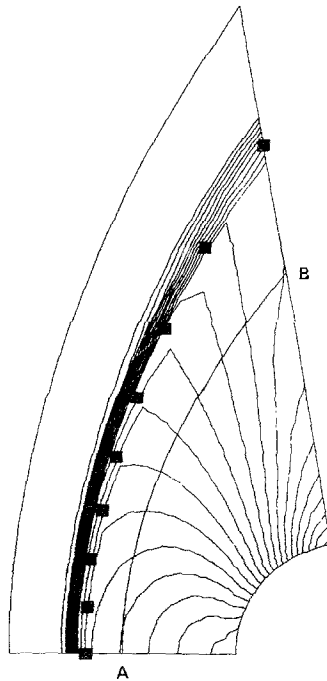
FIG. 9.   Isobars obtained at convergence for the cylinder with the Osher scheme.

contour lines can be seen to be continuous across the zonal boundary (AB); in fact, the lines seem to have an almost continuous slope across AB. The square symbols in this figure (and the following figures pertaining to the cylinder) represent the shock position predicted by another numerical approach in [13]. The captured shock is a little to the left of the predicted shock. This discrepancy is characteristic of the first-order-accurate Osher scheme and will disappear with the use of a second-order-accurate integration scheme [4]. Figure 10 shows the pressure contours obtained with the split-flux scheme. The quality of these contours in the vicinity of the zonal boundary is comparable to that obtained with the Osher scheme. The captured shock, however, is smeared to a greater extent. As before, the captured shock lies to the left of the predicted shock, a result of the first-order-accurate nature of the integration scheme.

A general-purpose zonal Euler code should have the capability of handling as many zones as necessary to cover the region of interest. To demonstrate the generality of the present zonal scheme and its applicability in a general-purpose zonal Euler code, the region of interest for the cylinder was divided into four zones instead of two zones (as in the previous case). The zones and the grids for each zone are shown in Fig. 11. A wide variation in cell shapes and sizes can be seen across each of the three zonal boundaries.
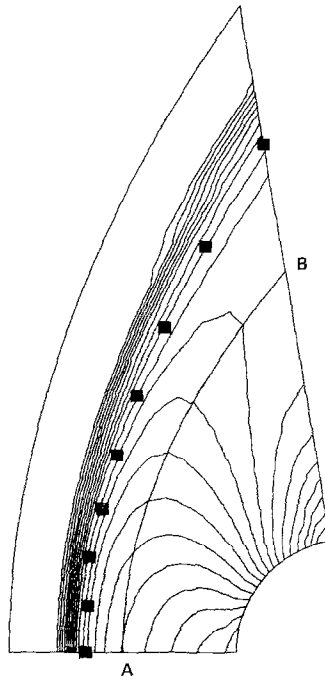
FIG. 10. Isobars obtained at convergence for the cylinder with the split-flux scheme.
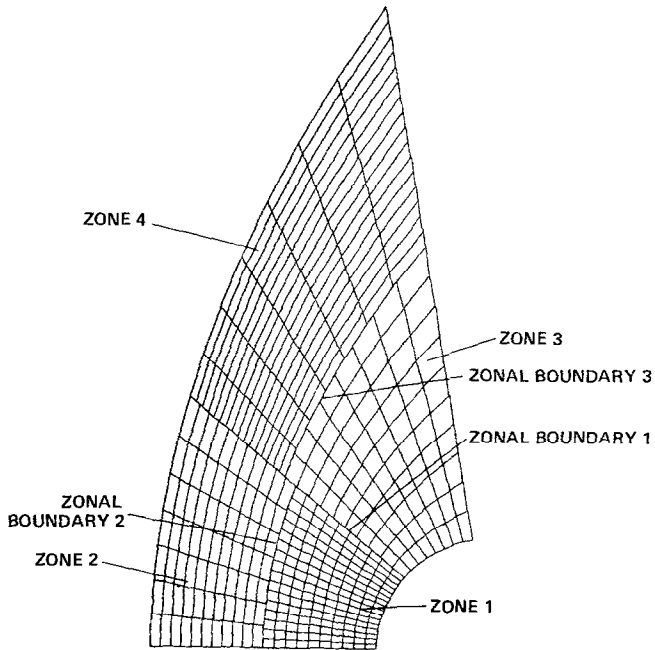

FIG. 11. Grid for four-zone cylinder calculation.

The values of the dependent variables at all the grid points were once again set equal to free-stream values initially. The bow shock associated with this flow field first appears at the body surface and then moves outward to its steady-state position. Figures 12–17 depict isobars and show the progression of the shock wave through the grid system as a function of the number of time-steps. Figure 17 shows the isobars obtained at convergence. The contours away from the shock in Figs. 12–17 are continuous across zonal boundaries. Small discontinuities in the contour lines are observed at zonal boundaries in the vicinity of the shock. This phenomenon is due to a difference in the interpolation subroutine used in the plotting package and the one used to enforce continuity of the dependent variables in the integration package (the contours in each zone are plotted independent of the other zones). The difference becomes evident only in large gradient regions, for example, near shocks. The smooth transition of the shock through all the zonal boundaries is apparent from Figs. 12–17. This smooth transition is possible because of the fully conservative nature of the zonal-boundary scheme.

Shock-Tube Problem

To determine the effect of the zonal-boundary conditions on the time-accuracy of a solution, the one-dimensional shock-tube problem was solved on a two-dimen-
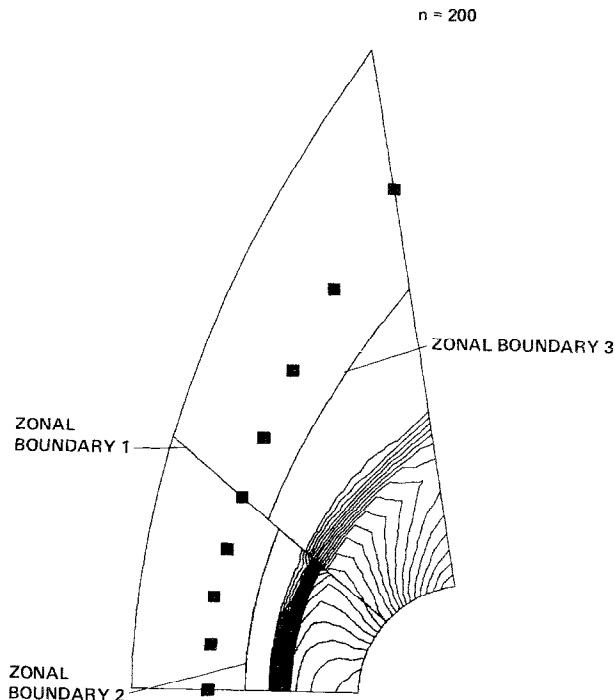

FIG. 12. Isobars after 200 integration steps for the cylinder, using the Osher scheme.
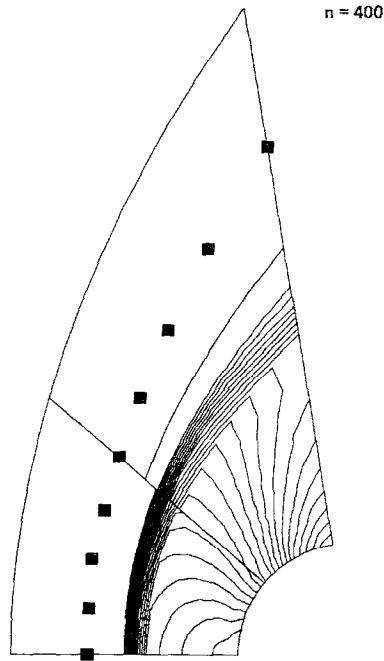
FIG. 13.   Isobars after 400 integration steps for the cylinder, using the Osher scheme.
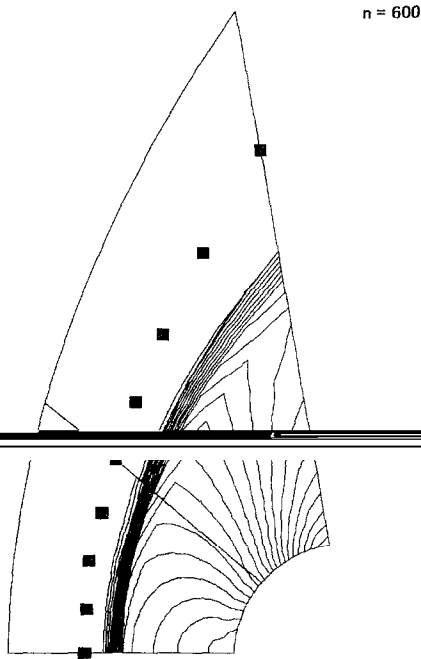

FIG. 14.   Isobars after 600 integration steps for the cylinder, using the Osher scheme.
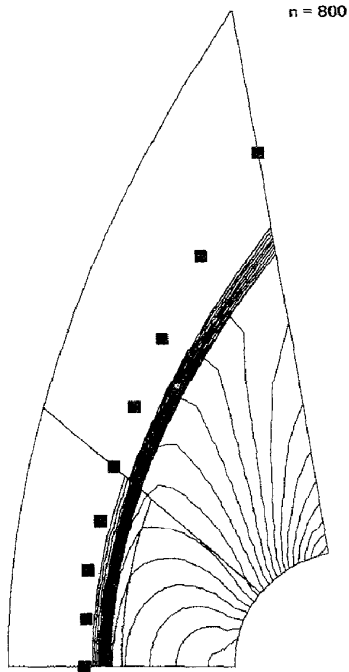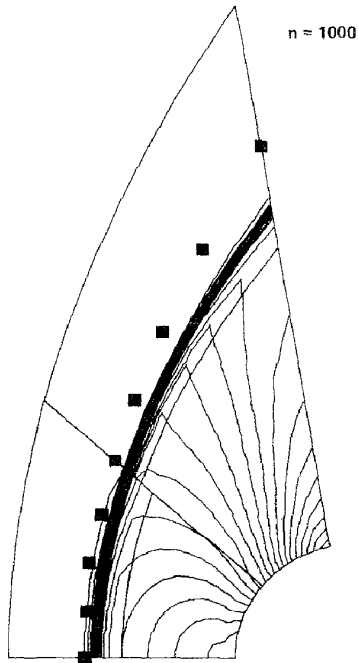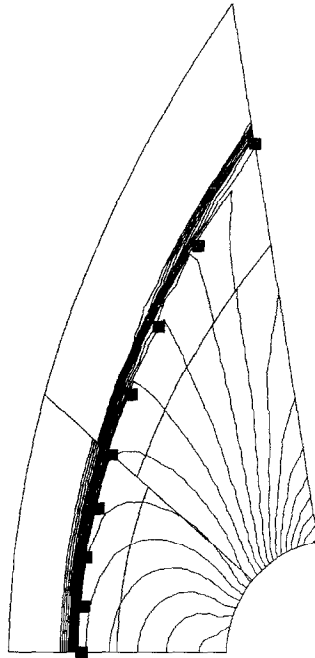
492

FIG. 15. Isobars after 800 integration steps for the cylinder, using the Osher scheme.

FIG. 16. Isobars after 1,000 integration steps for the cylinder, using the Osher scheme.

493

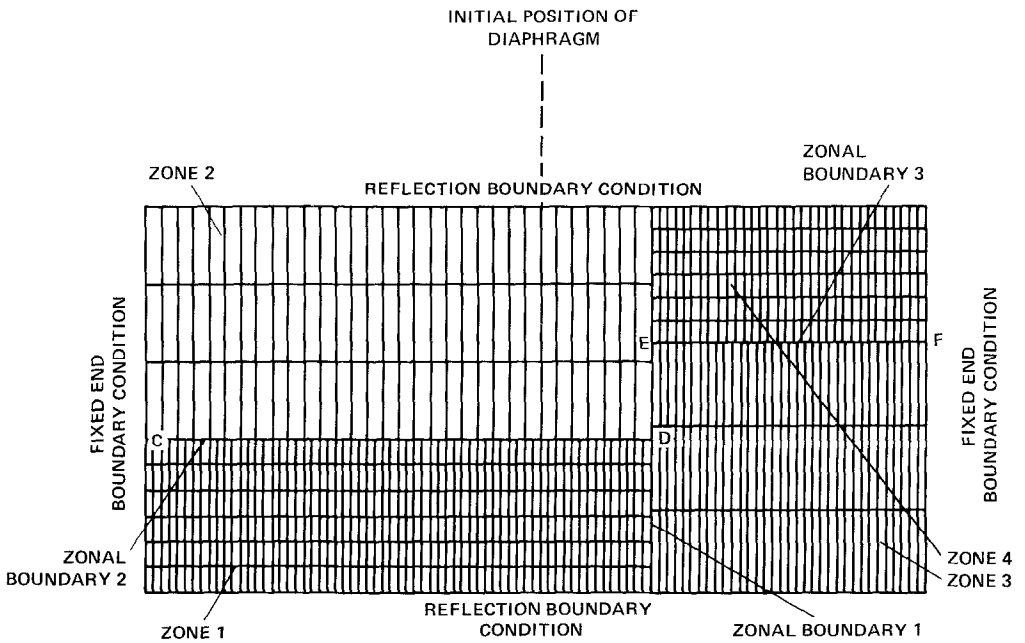FIG. 17. Isobars obtained at convergence for the cylinder, using the Osher scheme.

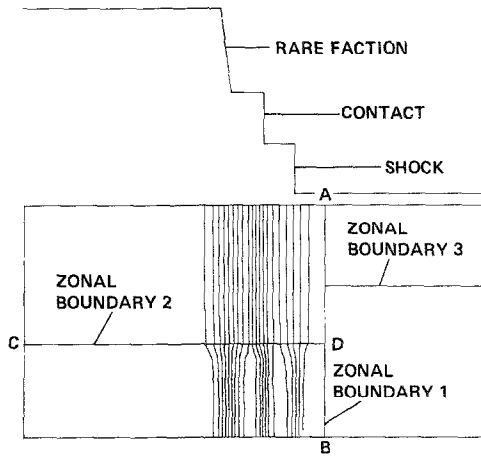FIG. 18. Grid for four-zone shock-tube calculation.

FIG. 19.   Isopycnics for the shock-tube problem soon after the rupture of the diaphragm.

sional grid. The region of interest was divided into four zones. The different zones and the grid for each zone are shown in Fig. 18. As in the previous case, cell volumes vary considerably across zonal boundaries. Initially, the diaphragm at the center separates the left and right states given by

$$\rho_L = 2.0, \qquad \rho_R = 1.0,$$

$$u_L = 0.0, \qquad u_R = 0.0,$$

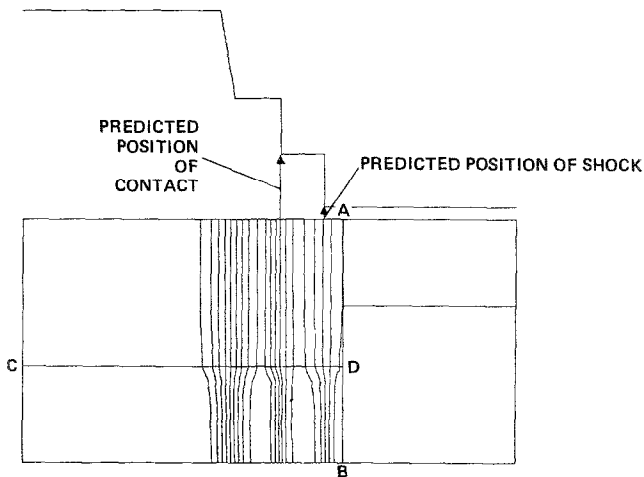$$v_L = 0.0, \qquad v_R = 0.0,$$

$$p_L = 2.0, \qquad p_R = 1.0.$$

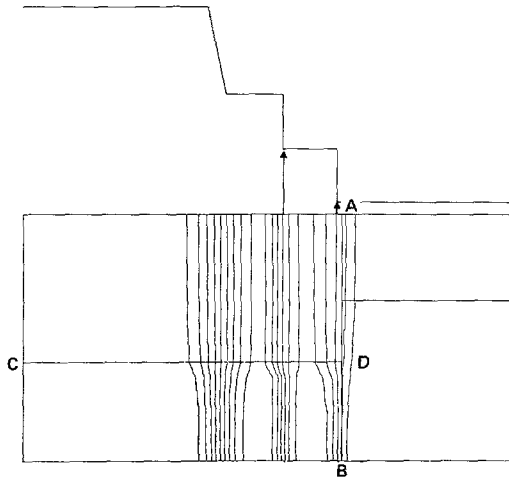FIG. 20.   Isopycnics for the shock-tube problem (shock just before AB).

FIG. 21.   Isopycnics for the shock-tube problem (shock passing through AB).

The diaphragm is then ruptured and a shock, contact, and rarefaction system is set up in the region with the shock and contact moving to the right and the rarefaction moving to the left. Reflection boundary conditions were imposed on the upper and lower boundaries because of the one-dimensional nature of the true solution. The two-dimensional calculation exhibits variations in both spatial dimensions because of the zonal boundaries and the smeared nature of the discontinuities. Fixed-end boundary conditions were used at the left and right boundaries.

Figures 19–23 show density contours at various positions in time. In the upper half of each of these figures the exact one-dimensional density profile is plotted as a function of x. The results presented in these figures were obtained with the Osher
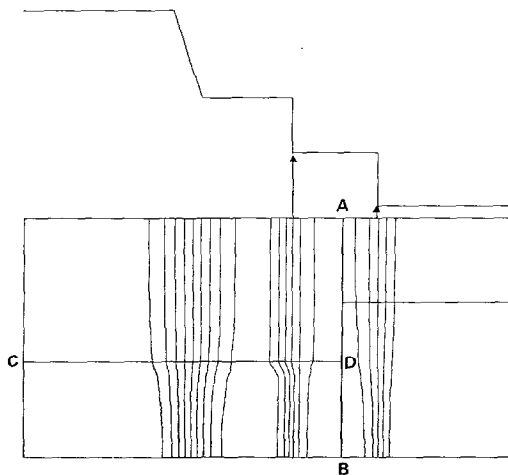

FIG. 22.   Isopycnics for the shock-tube problem (shock to the right of AB).

scheme. The first-order-accurate Osher scheme is extremely dissipative for transient problems with moving discontinuities, and, hence, the shock and contact profiles (in the form of density contours) shown in Figs. 19–23 are smeared to a greater extent than evidenced in the cylinder calculations. Figure 19 shows constant-density contours immediately after the rupturing of the diaphragm. Three distinct waves (shock, contact, and rarefaction) can be seen in this figure. Figure 20 shows the density contours just before the shock encounters the vertical zonal boundary (AB). Figure 21 shows the shock moving through AB with minimal distortion, and Fig. 22 shows the density contours just after the shock has moved through AB. Figure 23 shows the contact discontinuity beginning to pass through AB. An interesting feature in Figs. 19–23 is that the solution transitions from the low-error solution (closely spaced contour lines) to the high-error solution (widely spaced contour lines) across the zonal-boundary CD to satisfy the continuity requirement at this boundary.

Though it is difficult to say whether the calculated solution is time-accurate, some measure of the time-accuracy of the solution can be determined by finding the centers of the smeared shock and contact, and comparing the locations of these centers with the exact locations of the discontinuities. This has been done in Figs. 20–23; the arrows represent the centers of the smeared discontinuities. To the extent to which such a comparison can be held valid, it can be seen that the zonal calculation is time-accurate. The calculated position of the shock is close to the exact position of the shock before and after it passes through the zonal-boundary AB.

The shock-tube problem can be made to have an asymptotic solution in computational space by using a grid that expands in the x direction at the rate
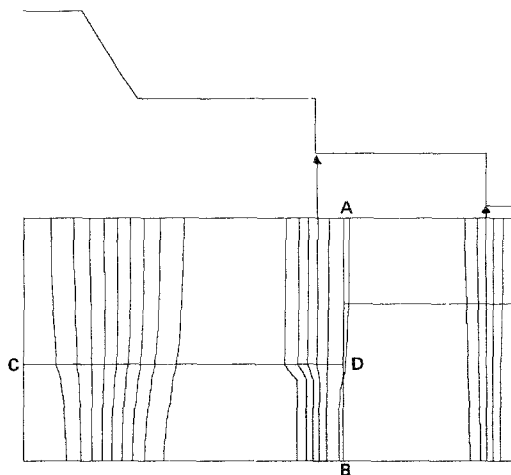
$$x_\tau = x.$$

FIG. 23. Isopycnics for the shock-tube problem (contact passing through AB).
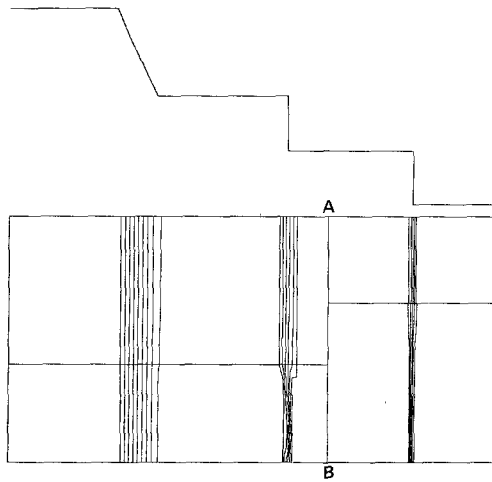
FIG. 24.   Isopycnics obtained at convergence for the shock-tube problem.

Since the solution then possesses an asymptotic limit in computational time, after the initial transients, the Osher scheme yields very sharp discontinuity profiles. Figure 24 shows the density contours obtained at convergence from such a calculation. The quality of the contour lines near the horizontal zonal boundaries is comparable to that obtained in the cylinder calculations.

Blast-Wave Diffraction by a Ramp

As stated earlier, one of the main advantages of being able to perform zonal calculations is that one can selectively refine the grid in certain areas of the flow region without having to maintain grid-line continuity across zonal boundaries. The problem of blast-wave diffraction by a ramp with its attendant complex shock patterns is a typical example of a problem requiring selective refinement of the grid. The grid used for the calculation performed in this study is shown in Fig. 25. The calculation was performed with an incident-shock Mach number of 7.1, a ramp angle of 49°, and a ratio of specific heats (γ) of 1.55. A double Mach reflection occurs for this choice of flow parameters. The discontinuities for this configuration include the incident shock, a kinked reflected shock, two Mach stems, and two slip lines. The region in which the triple point and Mach stems occur (the area covered by zone 2) requires a very fine grid to resolve all the flow features. A very coarse grid is sufficient for the area covered by zone 3 because the independent variables

The solution to the blast-wave diffraction problem is self-similar in time and, hence, can be made to have an asymptotic limit in computational space with the help of a similarity transformation. Details of the similarity transformation can be found in [14]. Figure 26 shows the isobars obtained at convergence with the Osher scheme. The kinked reflected shock (*ABC*), the incident shock (*CD*), and the first
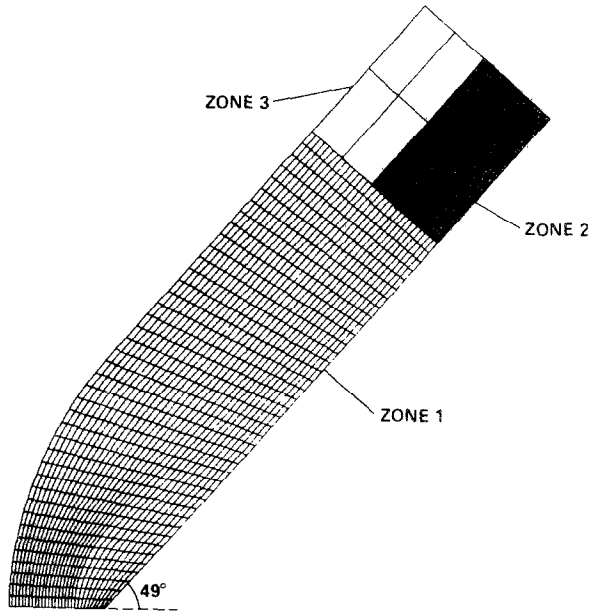
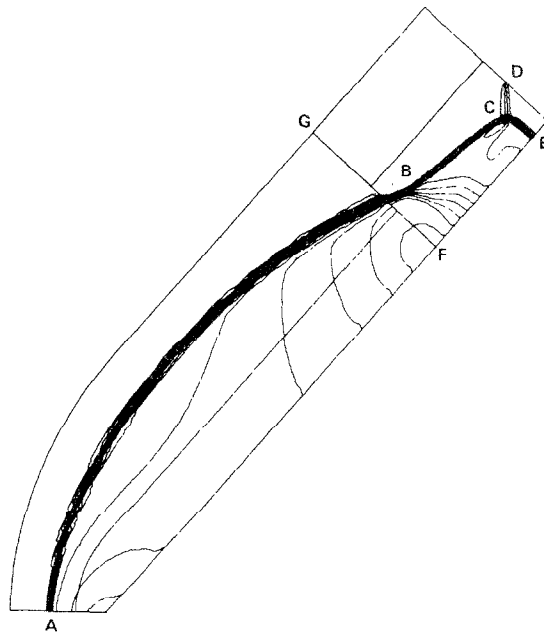FIG. 25.   Grid for three-zone blast-wave calculation.

FIG. 26.   Isobars obtained at convergence for the blast-wave problem using the Osher scheme.
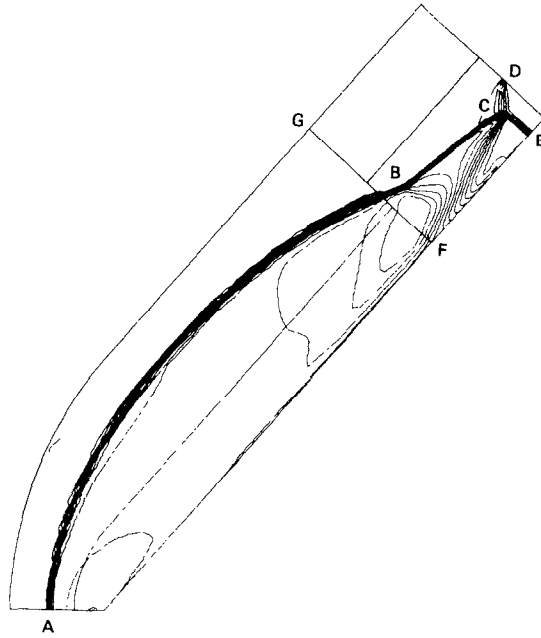
FIG. 27. Isopycnics obtained at convergence for the blast-wave problem using the Osher scheme.

Mach stem (CE) are seen to be captured very sharply. In addition, the second
Mach stem (much weaker than the first) can be seen emanating from the point B.
The reflected shock passes through the zonal boundary FG without any distortion;
it merely becomes thinner in zone 2 because of the fine grid used in this zone.
Figure 27 shows the density contours obtained at convergence. The additional
feature that this figure brings to light is the first slip line emanating from the triple
point C. The second slip line, which is suppose to emerge from point B, is much
weaker than all the other discontinuities and hence cannot be seen in this figure.

Conclusions

A conservative zonal-boundary scheme that permits the use of discontinuous
zonal grids has been developed for the Euler equations. The scheme is designed for
explicit, first-order-accurate integration schemes but can be extended to meet the
requirements of implicit and explicit second-order schemes. The integration techni-
ques used in this study are the Osher and split-flux schemes. The special logic
required to implement the zonal-boundary conditions was found to be fairly simple
to incorporate into existing codes.

Test problems that have been solved with the zonal technique include inviscid
supersonic flow over a cylinder, blast-wave diffraction by a ramp, and the one-

dimensional shock-tube problem. Results in the form of pressure and density contours are presented. The contours are observed to be continuous across zonal boundaries (except in the vicinity of discontinuities). Discontinuities were found to move freely and with minimal distortion through zonal boundaries. The zonal-boundary scheme was found to be stable even under severe test conditions such as strong discontinuities passing through the zonal boundaries. The results demonstrate the feasibility of using a zonal approach with discontinuous grids in solving complicated flow problems involving discontinuous solutions.

The first-order-accurate schemes used in this study are insufficient to produce very accurate results for a general class of problems. Also, the explicit nature of these schemes results in long convergence times when the grid used is sufficiently fine (because of Courant number limitations). Hence, the principal objective of current research is to extend the present zonal scheme so that it can be used with second-order accurate, implicit integration schemes.

APPENDIX: Error Analysis

The use of Eqs. (18) and (22) in calculating the fluxes $\hat{F}^{(2)}_{j,1/2}$, while maintaining flux conservation across the line CD (Fig. 6), does not result in free-stream preservation. It can be shown that defining $\hat{F}^{(2)}_{j,1/2}$ as

$$\hat{F}^{(2)}_{j,1/2}[Q, \eta^{(2)}_{j,1/2}] = \int_{E}^{F} \frac{\hat{F}^{(1)}_{l,3/2}(Q, \eta^{(2)}_{j,1/2}) \, ds}{[s^{(2)}_{j+1/2} - s^{(2)}_{j-1/2}]} \tag{A1}$$

will result in a free-stream preserving zonal scheme (private communication, S. R. Chakravarthy, Rockwell Science Center). However, Eq. (A1) is not flux-conserving (to the author's knowledge it is not possible to make the zonal scheme in its present form both flux-conserving and free-stream preserving). The metrics $\eta_{j,1/2}$ in Eq. (A1) can be obtained from the inverse metrics

$$\begin{aligned}
[x_{\xi^{(2)}}]_{j,1/2} &= (x)_T - (x)_U, \\
[y_{\xi^{(2)}}]_{j,1/2} &= (y)_T - (y)_U, \\
[x_{\tau^{(2)}}]_{j,1/2} &= \tfrac{1}{2}[(x_{\tau^{(2)}})_T + (x_{\tau^{(2)}})_U], \\
[y_{\tau^{(2)}}]_{j,1/2} &= \tfrac{1}{2}[(y_{\tau^{(2)}})_T + (y_{\tau^{(2)}})_U].
\end{aligned} \tag{A2}$$

The points T and U are shown in Fig. 6. The flux-conserving definition of the zonal fluxes [from Eq. (18)] is

$$\hat{F}^{(2)}_{j,1/2}[Q, \eta^{(2)}_{j,1/2}] = \int_{E}^{F} \frac{\hat{F}^{(1)}_{l,3/2}[Q, \eta^{(1)}_{l,3/2}] \, ds}{[s^{(1)}_{l+1/2} - s^{(1)}_{l-1/2}]}. \tag{A3}$$

Subtracting Eq. (A1) from Eq. (A3), we obtain the error vector (the vector that produces a drift in free-stream conditions) as

$$Er = \int_E^F \left\{ \frac{\hat{F}_{l,3/2}^{(1)}[Q, \eta_{l,3/2}^{(1)}]}{[s_{l+1/2}^{(1)} - s_{l-1/2}^{(1)}]} - \frac{\hat{F}_{l,3/2}^{(1)}[Q, \eta_{j,1/2}^{(2)}]}{[s_{j+1/2}^{(2)} - s_{j-1/2}^{(2)}]} \right\} ds. \qquad (A4)$$

An analysis of the quantity $\hat{F}^{(i)}[Q, \eta^{(i)}]/(x_\xi^2 + y_\xi^2)^{1/2}$ for the split-flux scheme shows that it can be written as

$$\frac{\hat{F}^{(i)}[Q, \eta^{(i)}]}{[x_{\xi^{(i)}}^2 + y_{\xi^{(i)}}^2]^{1/2}} = a\alpha^{(i)} + b\beta^{(i)} + c[\alpha^{(i)}]^2 + d[\alpha^{(i)}][\beta^{(i)}] + e[\beta^{(i)}]^2, \qquad (A5)$$

where a, b, c, d, and e are vector functions of x_τ, y_τ and the vector Q and are, thus, continuous across the zonal boundary. The terms $\alpha^{(i)}$ and $\beta^{(i)}$ are given by

$$\alpha^{(i)} = \frac{x_{\xi^{(i)}}}{[x_{\xi^{(i)}}^2 + y_{\xi^{(i)}}^2]^{1/2}},$$

$$\beta^{(i)} = \frac{y_{\xi^{(i)}}}{[x_{\xi^{(i)}}^2 + y_{\xi^{(i)}}^2]^{1/2}}, \qquad (A6)$$

and are also continuous across the zonal boundary (to the accuracy with which the metrics are calculated), because they represent the orientation of the zonal boundary. Making the approximations given in Eq. (19), substituting Eq. (A5) into Eq. (A4), and using the piecewise constant variation of $\hat{F}_{l,3/2}^{(1)}$ between grid points, the following is obtained:

$$Er = [s_{j+1/2}^{(2)} - s_{j-1/2}^{(2)}] \sum_{l=p}^{q} N_{j,l} \{ a_l[\alpha_l^{(1)} - \alpha_j^{(2)}] + b_l[\beta_l^{(1)} - \beta_j^{(2)}]$$

$$+ c_l[\alpha_l^{(1)} + \alpha_j^{(2)}][\alpha_l^{(1)} - \alpha_j^{(2)}] + d_l[\alpha_l^{(1)}\beta_l^{(1)} - \alpha_j^{(2)}\beta_j^{(2)}]$$

$$+ e_l[\beta_l^{(1)} + \beta_j^{(2)}][\beta_l^{(1)} - \beta_j^{(2)}] \}, \qquad (A7)$$

where the $N_{j,l}$ satisfy Eq. (8). Since the α's and β's are continuous across the zonal boundary we can write

$$\alpha_l^{(1)} = \alpha_j^{(2)} + K_l \frac{d\alpha}{ds} [s_{j+1/2}^{(2)} - s_{j-1/2}^{(2)}] + O[s_{j+1/2}^{(2)} - s_{j-1/2}^{(2)}]^2,$$

$$\beta_l^{(1)} = \beta_j^{(2)} + K_l \frac{d\beta}{ds} [s_{j+1/2}^{(2)} - s_{j-1/2}^{(2)}] + O[s_{j+1/2}^{(2)} - s_{j-1/2}^{(2)}]^2, \qquad (A8)$$

where the K_l are constants. Substituting Eq. (A8) into Eq. (A7) reduces Er to

$$Er = \left\{ \frac{d\alpha}{ds} C_1 + \frac{d\beta}{ds} C_2 \right\} [s_{j+1/2}^{(2)} - s_{j-1/2}^{(2)}]^2,$$

where C_1 and C_2 are vector constants. Thus, the drift in free-stream values introduced by using Eq. (18) instead of Eq. (A1) in evaluating $\hat{F}^{(2)}_{j,1/2}$ is due to a term that is second-order in magnitude. Since Er is primarily a function of $d\alpha/ds$ and $d\beta/ds$, the use of zonal boundaries that do not have large curvatures ($d\alpha/ds$ and $d\beta/ds$ are a measure of the curvature of the boundary) results in small values of the drift in the dependent variables. The drift in free-stream values is caused by the dual representation of the flux balance line CD in Fig. 6 (it is represented differently by the zonal boundary points of zones 1 and 2). The problem will disappear when a single consistent representation of CD that uses the zonal boundary points of both zones in defining the cells along the zonal boundary is used. This will mean that cell boundaries that lie along CD will in general consist of multiple line segments. This approach is currently being investigated.

REFERENCES

1. L. CAMBIER, W. GHAZZI, J. P. VEUILLOT, AND H. VIVIAND, "Une Approche par Domaines pour le Calcul d'Ecoulements Compressibles," Cinquieme Colloque International sur les Methodes de Calcul Scientifique et Technique, INRIA, Versailles, France, December 14–18, 1981.
2. K. A. HESSENIUS AND T. H. PULLIAM, "A Zonal Approach to Solution of the Euler Equations," AIAA Paper, No. 82-0969, St. Louis, Mo., 1982.
3. R. M. BEAM AND R. F. WARMING *AIAA J.* **16** (1978), 393.
4. M. M. RAI, K. A. HESSENIUS, AND S. R. CHAKRAVARTHY, *J. Comput. and Fluids* **12** (3) (1984), 161.
5. M. J. BERGER, "Adaptive Mesh Refinement for Hyperbolic Partial Differential Equations," Ph.D. thesis, Department of Computer Sciences, Stanford University, August 1982.
6. E. ATTA, "Component Adaptive Grid Interfacing," AIAA Paper, No. 81-0382, St. Louis, Mo., 1981.
7. about Aircraft Configurations," AIAA Paper, No. 82-1017, St. Louis, Mo., 1982.
8. J. L. STEGER, F. C. DOUGHERTY, AND J. A. BENEK, "A Chimera Grid Scheme," Mini-Symposium on Advances in Grid Generation, ASME Applied Bioengineering and Fluids Engineering Conference, Houston, Tex., June 20–22, 1983.
9. K. D. LEE, M. HUANG, N.J. YU, AND P. E. RUBBERT, "Grid Generation for Three-Dimensional Configurations," NASA CP-2166, 1980.
10. N. J. YU, "Transonic Flow Simulation for Complex Configurations with Surface Fitted Grids," AIAA Paper, No. 81-1258, St. Louis, Mo., 1981.
11. S. R. CHAKRAVARTHY AND S. OSHER, "Numerical Experiments with the Osher Upwind Scheme for the Euler Equations," AIAA Paper, No. 82-0975, St. Louis, Mo., 1982.
12. J. L. STEGER AND R. F. WARMING, *J. Comput. Phys.* **40** (1981), 263.
13. A. N. LYUBIMOV AND V. V. RUSANOV, "Gas Flows Past Blunt Bodies," NASA TT-F 715, 1973.
14. V. SHANKAR, P. KUTLER, AND D. A. ANDERSON, *AIAA J.* **16** (1) (1978), 4.